Title: Dipole Relaxation in Semiconducting Zn2−xMgxInV3O11 Materials (Where x = 0.0, 0.4, 1.0, 1.6, and 2.0)

Author: Tadeusz Groń, Monika Bosacka, Elżbieta Filipek, Sebastian Pawlus, Andrzej Nowok, Bogdan Sawicki, Henryk Duda, Jerzy Goraus

Citation style: Groń Tadeusz, Bosacka Monika, Filipek Elżbieta, Pawlus Sebastian, Nowok Andrzej, Sawicki Bogdan, Duda Henryk, Goraus Jerzy. (2020). Dipole Relaxation in Semiconducting Zn2−xMgxInV3O11 Materials (Where x = 0.0, 0.4, 1.0, 1.6, and 2.0). "Materials" (Vol. 13 (2020), Art. No. 2425), doi 10.3390/ma13112425

materials

MDPI

Article

Dipole Relaxation in Semiconducting $Zn_{2-x}Mg_xInV_3O_{11}$ Materials (Where x = 0.0, 0.4, 1.0, 1.6, and 2.0)

Tadeusz Groń [1], Monika Bosacka [2], Elżbieta Filipek [2], Sebastian Pawlus [1], Andrzej Nowok [1], Bogdan Sawicki [1], Henryk Duda [1] and Jerzy Goraus [1,*]

[1] August Chełkowski Institute of Physics, University of Silesia in Katowice, 40-007 Katowice, Poland; tadeusz.gron@us.edu.pl (T.G.); sebastian.pawlus@us.edu.pl (S.P.); andrzej.nowok@smcebi.edu.pl (A.N.); bogdan.sawicki@us.edu.pl (B.S.); henryk.duda@us.edu.pl (H.D.)

[2] Faculty of Chemical Technology and Engineering, Department of Inorganic and Analytical Chemistry, West Pomeranian University of Technology in Szczecin, 71-065 Szczecin, Poland; bossm@zut.edu.pl (M.B.); elafil@zut.edu.pl (E.F.)

* Correspondence: jerzy.goraus@us.edu.pl

Received: 20 April 2020; Accepted: 22 May 2020; Published: 26 May 2020

Abstract: This paper reports on the electrical and broadband dielectric spectroscopy studies of $Zn_{2-x}Mg_xInV_3O_{11}$ materials (where x = 0.0, 0.4, 1.0, 1.6, 2.0) synthesized using a solid-state reaction method. These studies showed *n*-type semiconducting properties with activation energies of 0.147–0.52 eV in the temperature range of 250–400 K, symmetric and linear I–V characteristics, both at 300 and 400 K, with a stronger carrier emission for the matrix and much less for the remaining samples, as well as the dipole relaxation, which was the slowest for the sample with x = 0.0 (matrix) and was faster for Mg-doped samples with x > 0.0. The faster the dipole relaxation, the greater the accumulation of electric charge. These effects were analyzed within a framework of the DC conductivity and the *Cole–Cole fit* function, including the solid-state density and porosity of the sample. The resistivity vs. temperature dependence was well fitted using the parallel resistor model. Our ab initio calculations also show that the bandgap increased with the Mg content.

Keywords: electrical properties; dielectric spectroscopy; relaxation processes

1. Introduction

It is known from the literature that double vanadates of the general formula $M^{II}_2M^{III}V_3O_{11}$, i.e., $M_2FeV_3O_{11}$ (M = Mg, Zn, Ni), $M_2CrV_3O_{11}$ (M = Mg, Zn), and $M_2InV_3O_{11}$ (M = Mg, Zn, Co), crystallize in the triclinic system [1–6]. These compounds may be used as catalysts or photo-catalysts in various chemical processes. In particular, complex metal oxides based on iron ions are the most attractive objects for investigation. For example, in functional hexaferrite $BaFe_{12-x}DI_xO_{19}$ (DI = Al^{3+}, In^{3+} $0.1 \leq x \leq 1.2$) solid solutions with an increase in Al^{3+} and In^{3+} ion concentrations, the natural ferromagnetic resonance frequency is shifted from 51 GHz to 61 GHz and from 50.5 GHz to 27 GHz, respectively [7]. In M-type hexaferrite $BaFe_{12-x}In_xO_{19}$ (x = 0.1, 1.2) samples, an influence of structural parameters on the temperature behavior of Fe^{3+}(i)–O^{2-}–Fe^{3+}(j) (i, j = 1, 2, 3, 4, 5) indirect superexchange interactions was established [8]. In turn, in nanosized ferrites of $Sr_{0.3}Ba_{0.4}Pb_{0.3}Fe_{12}O_{19}/(CuFe_2O_4)_x$ (x = 2, 3, 4, and 5), non-linear behavior of the microwave characteristics was observed [9].

A solid solution of a $Zn_{2-x}Mg_xInV_3O_{11}$ composition was found to form in the $Zn_2InV_3O_{11}$–$Mg_2InV_3O_{11}$ system [10]. The phases with x = 0.0, 0.4, 1.0, 1.6, and 2.0 were obtained using solid-state reactions. The solid solution under study crystallized in the triclinic system. Its unit cell parameters *a* and *b* increased, while the unit cell parameter *c* decreased with an increasing magnesium

content [10]. The solid-state density values obtained experimentally (d_{exp}) and calculated (d_{cal}) based on X-ray diffraction (XRD) data decreased as a function of the degree of Mg^{2+} ions' incorporation in the crystal lattice of $Zn_2InV_3O_{11}$ [10], where a good agreement was shown between d_{exp} and d_{cal}. The level of porosity of $p_l \approx 1.67\%$ determined using the formula $p_l = (1 - d_{exp}/d_{cal})$ did not depend on the magnesium content x. Similar behavior was found for $M_2FeV_3O_{11}$ compounds (where M = Mg, Ni, Pb) [11]. Scanning electron microscopy (SEM) images of $Zn_{2-x}Mg_xInV_3O_{11}$ samples with x = 0.0, 1.0, and 2.0 showed almost identical shapes and sizes to the crystallites of the compounds (x = 0.0 and 2.0), while the crystallites of the solid solution (x = 1.0) had a similar shape but were much larger [10]. The infrared spectroscopy measurements showed that all recorded spectra were similar and contained the stretching vibrations of V–O bonds in highly distorted VO_4 and VO_5 polyhedra in the wavenumber range of 1000–900 cm^{-1} [1,2,5,12,13]. Next, in the absorption band covering the range 900–400 cm^{-1}, the stretching vibrations were ascribed to the moderately distorted VO_4 tetrahedra or to stretching vibrations in ZnO_x and MgO_x [1,13–16]. Recently, the preliminary results of magnetic and dielectric measurements of $Zn_{2-x}Mg_xInV_3O_{11}$ phases with x = 0.0, 0.4, and 1.6 showed diamagnetic behavior above room temperature and a strong increase in the relative electrical permittivity as the magnesium content increased [17].

Here, we present the results of electrical measurements and broadband dielectric spectroscopy studies of $Zn_{2-x}Mg_xInV_3O_{11}$ materials (where x = 0.0, 0.4, 1.0, 1.6, 2.0). The samples under study were almost identical to those described in Bosacka and Filipek [10], which contains all the details of the conducted synthesis, morphology, and X-ray phase analysis. The main motivation of this work was to examine the dielectric relaxation in the frequency representation using the sum of the conductivity part and the *Cole–Cole fit* function.

2. Experimental and Calculation Details

2.1. Synthesis and Phase Analysis

Preliminary studies of the reactions occurring in the $ZnO–MgO–V_2O_5–In_2O_3$ system allowed for synthesizing a series of solid solutions with the formula $Zn_{2-x}Mg_xInV_3O_{11}$ (x = 0.0, 0.4, 1.0, 1.6, 2.0) [10]. Synthesis of the solid solution was performed using the solid-state reaction method described in Bosacka and Filipek [10]. XRD analysis of all samples showed them to be monophasic. XRD patterns of single-phase samples containing $Zn_{2-x}Mg_xInV_3O_{11}$ were the same as those recorded in Bosacka and Filipek [10]. Tests of all samples synthesized in this study also confirmed that a continuous solid solution with the general formula $Zn_{2-x}Mg_xInV_3O_{11}$ crystallized in the triclinic system and the parameters of its unit cell *a* and *b* increased, while the parameter *c* decreased with increasing magnesium content.

The sample morphology observed on the scanning electron microscopy images showed that the crystal phases were irregular polyhedra and their average size was about 1–5 μm. As an example, Figure 1 shows an SEM image of a sample containing $Zn_{2-x}Mg_xInV_3O_{11}$ with x = 1. The results of the experimental determination of the crystals' composition using Energy Dispersive X-ray (EDX) analysis of this monophase sample showed that the Zn:Mg:In:V ratios were near 1:1:1:3 (on average: 17.3 at% Zn, 15.5 at% Mg, 16.5 at% In, and 50.7 at% V), which corresponded to the values from the formula $ZnMgInV_3O_{11}$.

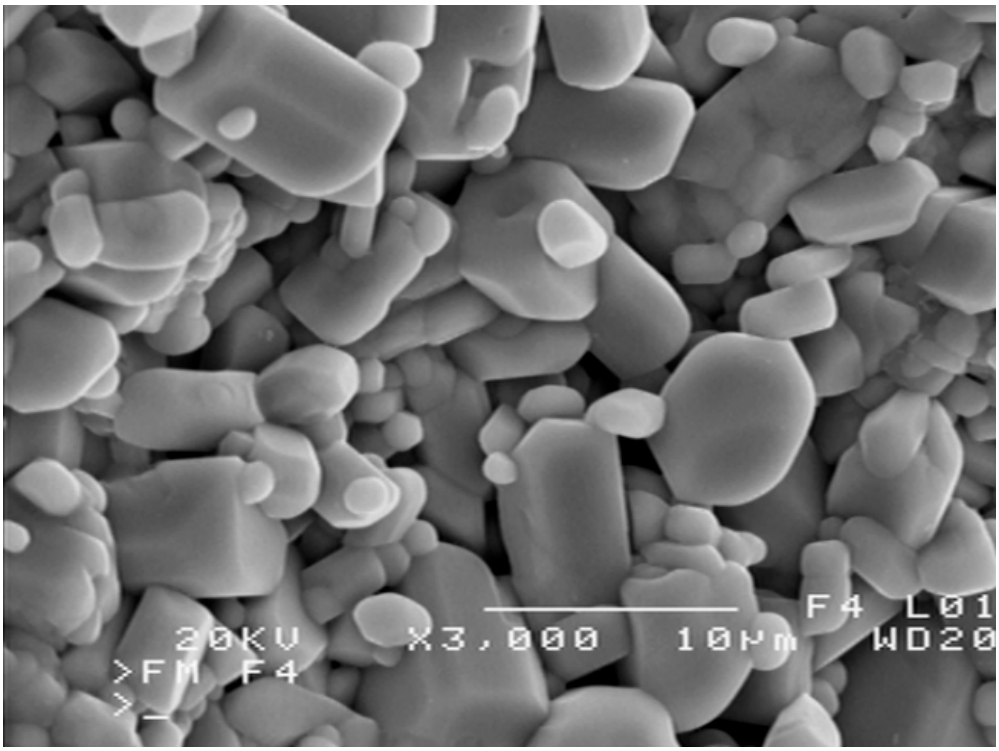

Figure 1. SEM image of $ZnMgInV_3O_{11}$.

The densities of the samples (d_{exp}) were determined using a gas pycnometer (Ultrapyc 1200e, Quantachrome Instruments, Boynton Beach, FL, USA) and argon with a 5 N purity was used as the pycnometric gas. Its dependence on x in Figure 2 is the same as in Bosacka and Filipek [10].

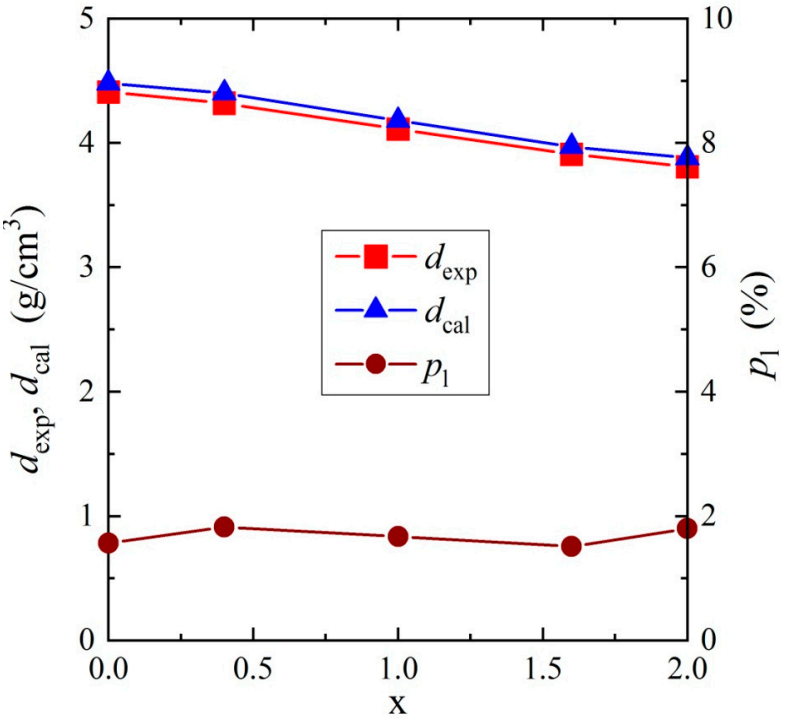

Figure 2. Experimental, d_{exp}, and calculated, d_{cal}, solid-state density and porosity level, p_l, as a function of the content x of $Zn_{2-x}Mg_xInV_3O_{11}$. Calculated data is taken from Bosacka and Filipek [10].

2.2. Electrical Measurements

The electrical conductivity σ(T) in the temperature range of 80–400 K and the I–V characteristics at 300 and 400 K were measured using the DC method using a KEITHLEY 6517B Electrometer/High Resistance Meter (Keithley Instruments, LLC, Solon, OH, USA). The thermoelectric power S(T) was measured in the temperature range of 300–400 K using a Seebeck Effect Measurement System (MMR Technologies, Inc., San Jose, CA, USA). The broadband dielectric spectroscopy measurements were carried out using pellets that were polished and sputtered with (≈80 nm) Ag electrodes in a frequency range from 2×10^2–2×10^6 Hz using an LCR HITESTER (HIOKI 3532-50, New York, NY, USA) and in the temperature range 80–400 K. For the electrical measurements, the powder samples were compacted in a disc form (10 mm in diameter and 1–2 mm thick) using a pressure of 1.5 GPa; then, they were sintered for 2 h at 923 K. The electrical and thermal contacts were made using a silver lacquer mixture (Degussa Leitsilber 2000, is Degussa Gold und Silber, Munich, Germany).

2.3. Density Functional Calculations

We performed the band structure calculations based on the density functional theory (DFT) using CRYSTAL software (CRYSTAL17, University of Turin, Turin, Italy) [18] for three representatives of the $Zn_{2-x}Mg_xInV_3O_{11}$ series (x = 0.0, 1.0, 2.0) since due to the method used, we could only substitute particular atoms in the unit cell, and hence fractional substitution was not possible. The CRYSTAL software uses a Gaussian type basis set: for In, we used the basis employed in Rothballer et al. [19], and for the remaining lighter elements, we used the double-zeta basis, as published in Vilela Oliveira et al. [20]. We used the exchange-correlation potential as proposed in Perdew et al. [21] and 260 k-points in the irreducible wedge of the Brillouin zone. We relaxed the atomic positions (using default criteria in CRYSTAL) but the lattice parameters were taken from the XRD measurements. The unit cells of the considered compounds were large and low-symmetry with 17 inequivalent Wyckoff positions. Hence, the lattice dynamics or elastic parameters were not studied here; we were only interested in the change of the semiconducting bandgap width relative to the Mg content.

3. Results and Discussion

3.1. Electrical Properties and Density of States

The results of the electrical measurements of the solid solution of $Zn_{2-x}Mg_xInV_3O_{11}$ (x = 0.0, 0.4, 1.0, 1.6, and 2.0) composition showed semiconducting properties with an activation energy of 0.2–0.3 eV in the temperature range of 250–400 K, i.e., in an intrinsic region (Figure 3) and with n-type conductivity (Figure 4). The I–V characteristics, measured at 300 and 400 K (Figure 5), showed symmetric and linear behavior with more carrier emissions for the matrix ($Zn_2InV_3O_{11}$) and much less for the remaining samples.

In Figure 5, the 300 (a) and 400 K (b) plots of the matrix (x = 0.0) compared to the other phases (x > 0.0) indicated the existence of vanadium ions with mixed valences in the matrix. With increased magnesium content, this mixed valence of vanadium ions was reduced. Generally, small values of the electrical conductivity in the temperature range of 80–400 K and low electron emissions of the phases under study (Figures 3 and 5) indicated a good dielectric behavior, which may have been due to the existence of centers trapping current carriers lying in the deep donors. The energy required for the creation of a vacancy depends on the bond type. The stronger the bond, the higher the energy needed for the creation of a vacancy. Similar behavior in $AgY_{1-x}(Gd,Nd)_x(WO_4)_2$ was observed [22].

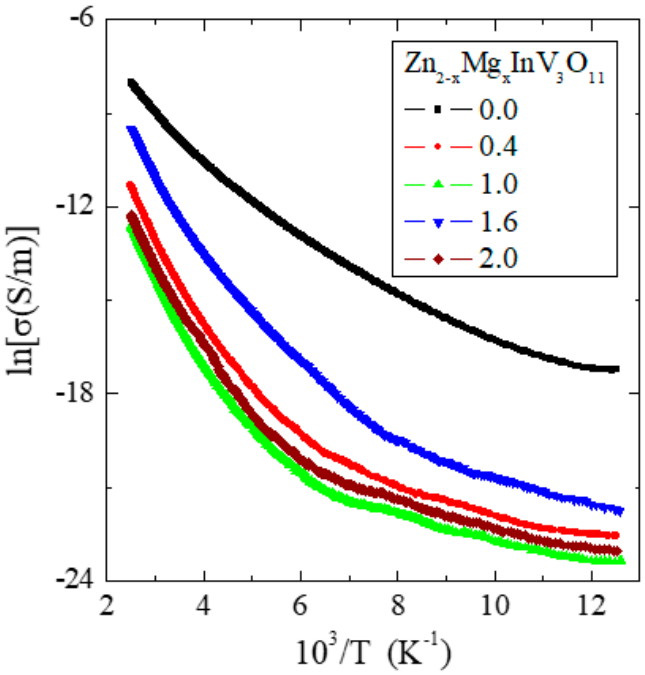

Figure 3. Electrical conductivity (lnσ) vs. reciprocal temperature $10^3/T$ of $Zn_{2-x}Mg_xInV_3O_{11}$.

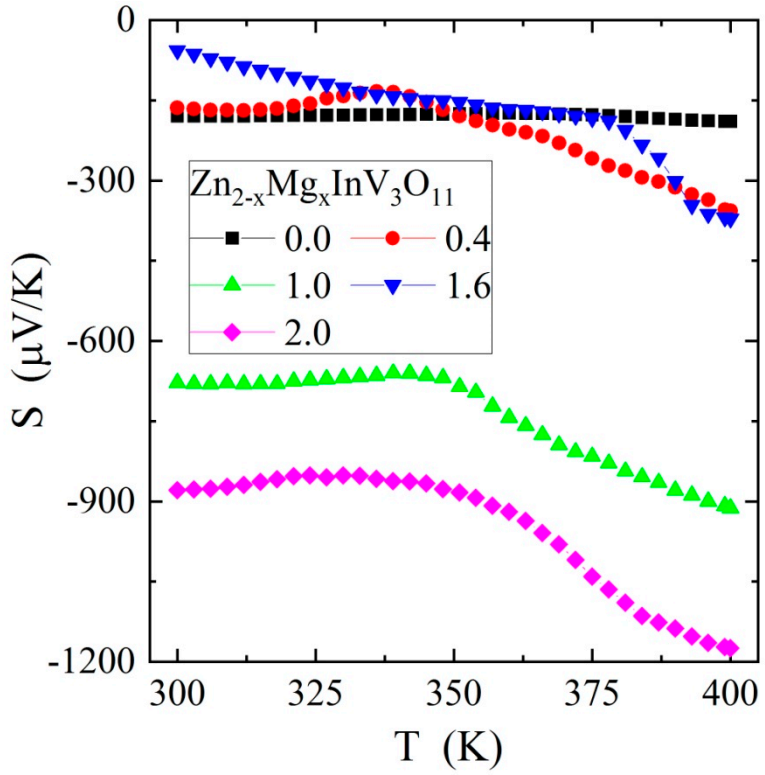

Figure 4. Thermoelectric power S vs. temperature T of $Zn_{2-x}Mg_xInV_3O_{11}$.

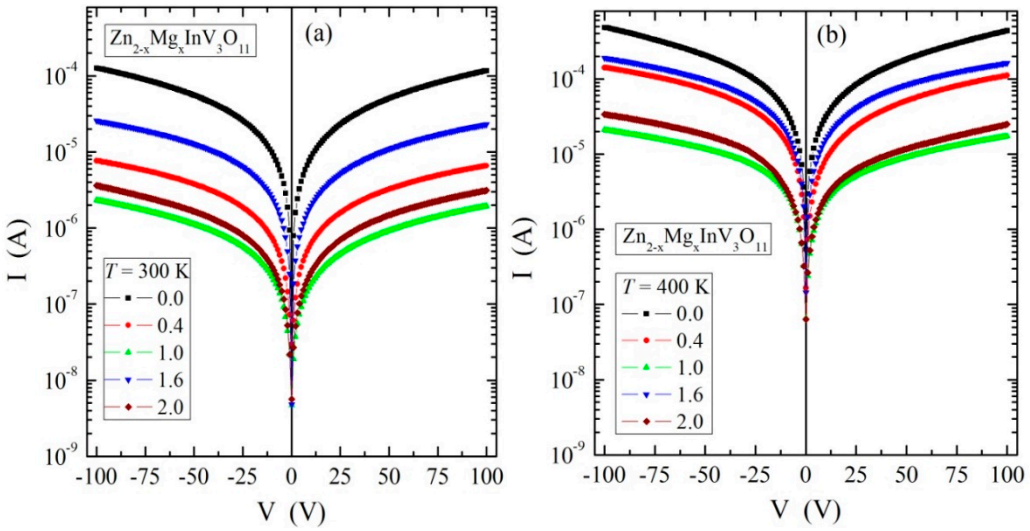

Figure 5. The I–V characteristics at 300 (**a**) and 400 K (**b**) of $Zn_{2-x}Mg_xInV_3O_{11}$.

It is worth noting that if the activation law properly described the resistivity vs. temperature dependence of these materials, the ln(σ) vs. 1/T curve shown in Figure 3 should be a straight line. We see that this is not the case. A simple explanation can be provided based on the parallel resistor model (PRM) [23,24], where we assume that the resistivity vs. temperature dependence ρ(T) of these materials consists of two parts, which are connected in parallel. One is described by the activation law $\rho_0 \exp\left(\frac{\Delta}{2kT}\right)$ and the second is constant relative to temperature $\rho_p = const$. Here, Δ denotes a bandgap in the density of states between the conduction and valence states and k is the Boltzmann constant. This model (Equation (1)), with ρ_0, ρ_p, and Δ as fitting parameters, was recently successfully employed to explain the semiconducting properties of cisplatin [25].

$$\rho(T) = \frac{\rho_p \rho_0 \exp\left(\frac{\Delta}{2kT}\right)}{\rho_p + \rho_0 \exp\left(\frac{\Delta}{2kT}\right)} \quad (1)$$

In Figure 6, we show the measured resistivity vs. temperature (empty symbols) with the PRM fit (dashed line). We see that this model almost perfectly describes the resistivity vs. temperature curve of $Zn_{2-x}Mg_xInV_3O_{11}$ series over a broad temperature range. The fit parameters are given in Table 1. The pristine $Zn_2InV_3O_{11}$ compound had the narrowest bandgap of about 0.154 eV, whereas compositions where Mg replaced Zn atoms had wider bandgaps of about 0.3–0.517 eV. Moreover, the width of the bandgap did not change monotonically with Mg content for those compounds. However, it should be noted that the parallel resistivity ρ_p also changed significantly, over four orders of magnitude. This ρ_p represents the current leakage, which might be related to grain size, off-stoichiometry, and sample synthesis conditions, and not to the inherent properties of these compounds. Probably, it is also strongly affected by the pressure used to compress the samples during their synthesis. We determined the total density of states based on density functional theory (DFT) calculations (see Figure 7) for three members of the series $Zn_{2-x}Mg_xInV_3O_{11}$ (x = 0, 1, 2). The obtained ground state was non-magnetic, in agreement with our preliminary experimental data mentioned in the introduction. We see that width of the bandgap increased with Mg content and the narrowest bandgap was observed for the pristine $Zn_2InV_3O_{11}$ compound. This agrees well with our resistivity data. One might notice that the bandgap obtained from the DFT calculations was wider than the one obtained from fitting the experimental ρ(T) curve. This is a little bit atypical, as usually the DFT calculations underestimate the width of the bandgap. Here, we explain this phenomenon in terms of the complicated structure of the $Zn_{2-x}Mg_xInV_3O_{11}$ unit cell, as well as the residual states that are formed in the bandgap due to atomic disorder [26].

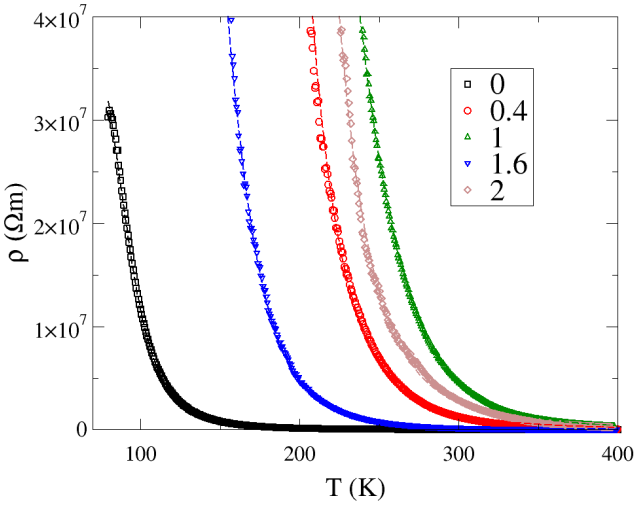

Figure 6. The resistivity of $Zn_{2-x}Mg_xInV_3O_{11}$ (empty symbols) fitted using the parallel resistor model [23].

Table 1. Parallel resistor model fit of $Zn_{2-x}Mg_xInV_3O_{11}$ (as seen in Figure 6).

x	ρ_0 (Ωm)	ρ_p (10^7 Ωm)	Δ (eV)
0	2146.7	3.95	0.154
0.4	241.5	8.46	0.444
1.0	210.4	1.07	0.517
1.6	696.7	9.97	0.306
2.0	638.8	10912	0.428

ρ_0 and ρ_p are the parameters describing the two resistivities; the former changes with temperature according to the activation law, while the latter is constant with temperature. Δ is the bandgap between the valence and conduction states (see Equation (1)).

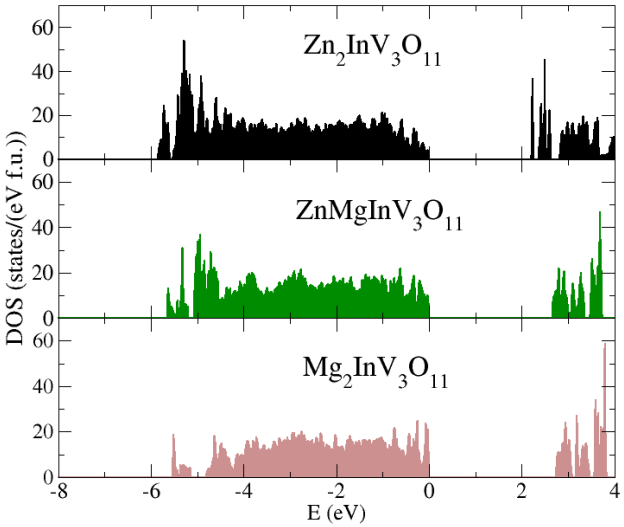

Figure 7. The total density of states (DOS) calculated for $Zn_{2-x}Mg_xInV_3O_{11}$ (x = 0, 1, 2).

3.2. Dielectric Results

The results of the broadband dielectric spectroscopy measurements of $Zn_{2-x}Mg_xInV_3O_{11}$ for the representative x = 0.0, 1.0, and 2.0 displayed in Figure 8a–f showed a strong increase in the relative electrical permittivity, ε_r, above 150 K, irrespective of the magnesium content in the sample. On the other hand, the maximum value of ε_r for the lowest frequencies (marked with vertical arrows in Figure 8a–c) increased with the magnesium content. With the increase in the frequency of the electric field, both ε_r and the loss tangent tanδ strongly decreased. In particular, a high loss was observed at low

frequencies, which is characteristic of Joule–Lenz-type losses (Figure 8d–f). It should be noted that tanδ at 500 Hz crossed the value of 1 at ≈175 K for x = 0, whereas for samples with a higher concentration of magnesium, this temperature increased to ca. ≈250 K for x = 1.0 and x = 2.0 (see horizontal dashed lines in Figure 8d–f).

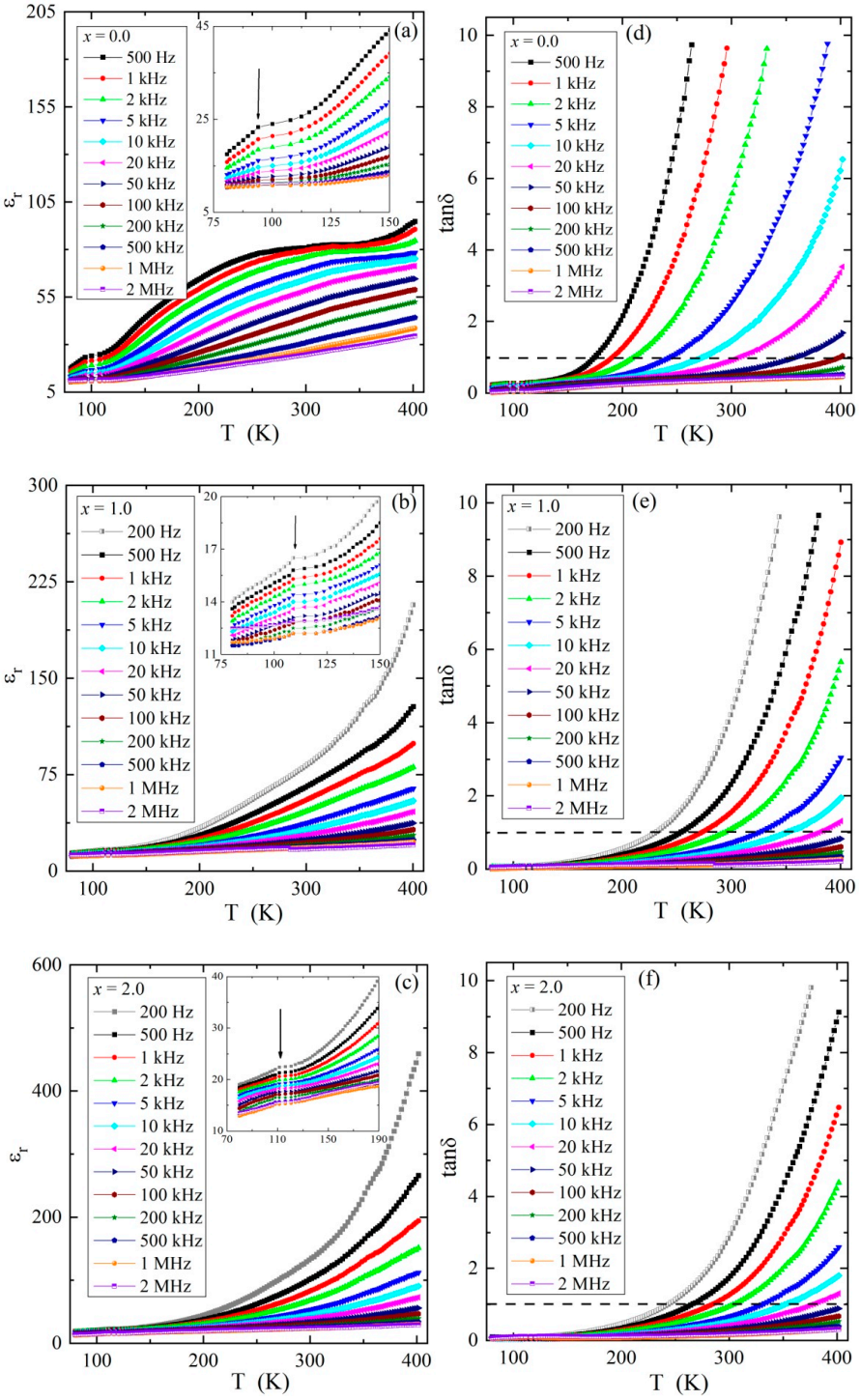

Figure 8. Dielectric constant ε_r (x = 0.0 for (**a**), x = 0.1 for (**b**), x = 0.2 for (**c**)) and loss tangent tanδ (*x* = 0.0 for (**d**), x = 0.1 for (**e**), x = 0.2 for (**f**)) vs. temperature T of $Zn_{2-x}Mg_xInV_3O_{11}$ in the frequency range 200 Hz to 2 MHz. Insets: There was a change in the T-dependence of ε_r in the vicinity of 94 K (for x = 0.0 in (**a**)), 109 K (for x = 1.0 in **b**), and 111 K (for x = 2.0 in (**c**)), which are marked with vertical arrows. Horizontal dashed lines in the tanδ vs. T dependences indicate the value of tanδ = 1.

The above-mentioned dielectric properties could be interpreted as being related to a relaxation process, such as in Maxwell-Wagner [27] or Jonscher [28], which was strongly obscured by the DC conductivity with an activation energy of 0.2–0.3 eV in the intrinsic region. A similar relaxation process has been found in $Sr_2InV_3O_{11}$ [29], $M_2FeV_3O_{11}$ (M = Mg, Zn, Pb, Co, Ni) [11], and $Nb_6VSb_3O_{25}$ compounds with an activation energy of 0.75 eV [30,31]. From Figure 8, one can see that the variation in ε_r strongly depended on the content of magnesium ions, which reduced the number of vanadium ions with mixed valence. Finally, this led to the accumulation of electric charge in the deep trapping centers [32] lying under the bottom of the conduction band. A natural source of these traps can be grain boundaries with depletion layers of adjacent grains, as it has been observed for ZnO varistors [33], Nb_2VSbO_{10} compounds [34], and some copper/cobalt and rare-earth metal tungstates [35], as well as for (Co,Mn)$Pr_2W_2O_{10}$ materials [36].

3.3. Dielectric Analysis

It must be noted that, as already presented above, both the ε_r and tanδ as functions of temperature provide only limited information about the electric properties of the materials. Let us start the dielectric analysis of the temperature dependence of the dielectric permittivity, $\varepsilon_r(T)$, of two representative samples with x = 0.0 and 2.0, for which the transition region is marked with an arrow in Figure 8a,c. As can be seen, ε_r declined with a decrease in temperature and a decrease in frequency for both samples with x = 0.0 and 2.0. However, this relationship was nonlinear in nature, which can indicate the existence of dipole relaxation. Unfortunately, this weekly visible dipole relaxation was impossible to analyze in the plots with varying temperatures. Moreover, there was a change in the *T*-dependence of ε_r in the vicinity of 100 K (for x = 0.0) and 111 K (for x = 2.0, visible in the inset of Figure 8a,c), which could indicate a transition in the materials. Interestingly, the transition's temperature for each sample remained independent of the frequency, which excludes a relaxation-type transition as the cause.

Because the dipole relaxation was poorly detectable with changing temperatures, the data were converted to depend on frequency. It must be mentioned that frequency dependencies of dielectric permittivity, $\varepsilon'(v)$, and dielectric loss, $\varepsilon''(v)$, are interrelated via Kramers–Kronig relations [37]; therefore, it is not necessary to analyze both parts of the complex dielectric permittivity, $\varepsilon^*(v)$. Consequently, only $\varepsilon''(v)$ data were used for further calculations. The dielectric loss spectra for samples with x = 0.0 and 2.0 are shown in Figure 9. In this representation, two processes are visible for both samples. Linear bending with decreasing frequency was observed at higher temperatures, which shifted to lower frequencies with cooling (Figure 9a,c). This process was related to the ion conductivity of the material. Additionally, a faster relaxation process emerged with the decrease in temperature at higher frequencies, which is visible as a shoulder in the conductivity part (Figure 9b,d), and developed into a relaxation peak with further cooling (Figure 9d). This relaxation shifted to lower frequencies with cooling, which is marked using arrows in Figure 8c,d. Both processes were observed in each investigated sample; however, the degrees of development of the dipole relaxation from the conductivity part were different for different samples (see Figure 10 below).

It has to be emphasized that dipole relaxation came into the experimental frequency window at different temperatures for each sample, and for that reason, the time scale for this process should change for different samples at comparable temperatures. This was reflected in Figure 10a, where the $\varepsilon''(v)$ spectra were compared for three similar temperatures for samples with x = 0.0 and 2.0. It is clear from this figure that the time scales of the dipole relaxation process in the material with x = 0.0 was much slower than for the sample with x = 2.0 for the same temperature conditions. As shown in Figure 10b, such a scheme was also observed for other samples: with the increasing content of dopant, the dipole relaxation became faster for the same temperature of ≈89 K. It was noticeable that the amplitude of the relaxation in the sample with x = 0.0 was about one order of magnitude higher in comparison to the others. The spectra for the sample with x = 0.4 were not compared due to the poor quality of the data for this sample in the temperature range in which the relaxation was observed.

This poor quality may be related to the morphology of sample solutions, whose grain size was much larger than the grain size of the samples that were compounds.

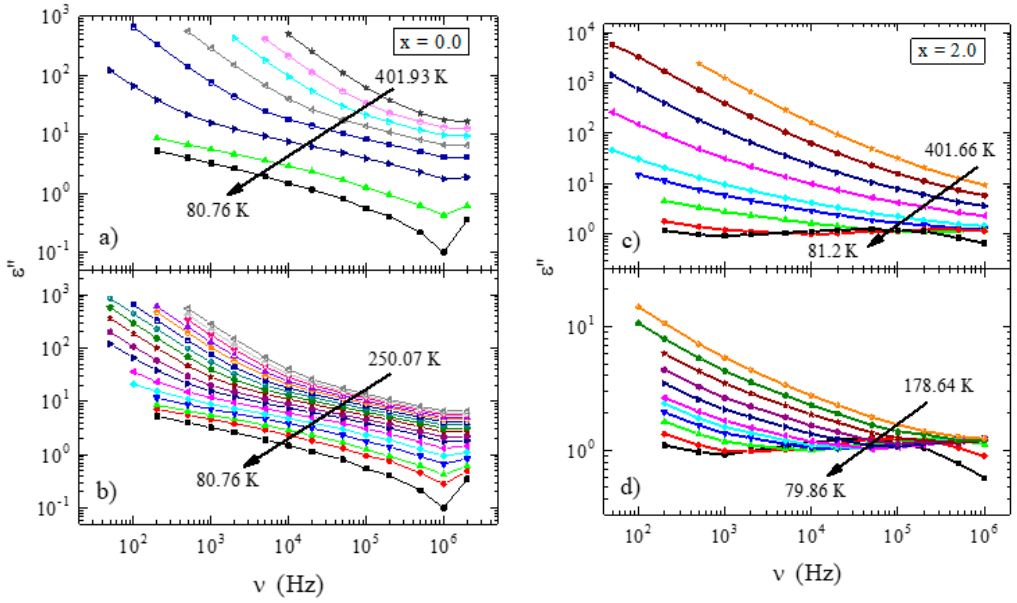

Figure 9. Frequency dependence of the dielectric loss spectra presented for various temperatures, $\varepsilon''(\nu)$, for x = 0.0 with $\Delta T \approx 50$ K (20 K between two lowest temperatures) (**a**) and with $\Delta T \approx 10$ K (**b**), and for x = 2.0 with $\Delta T \approx 50$ K (10 K between two lowest temperatures) (**c**) and with $\Delta T \approx 10$ K (**d**). Arrows indicate the direction of the temperature evolution of the relaxation process with cooling.

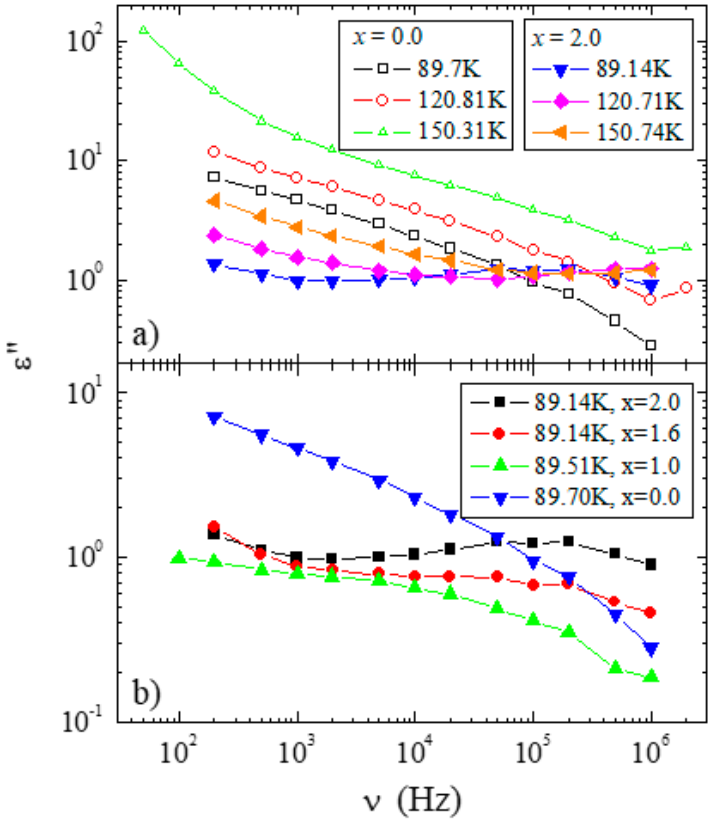

Figure 10. (**a**) A comparison of the dielectric loss spectra collected for the same temperatures and samples for x = 0.0 (empty symbols) and x = 2.0 (full symbols). (**b**) A comparison of the loss spectra for different samples at ≈89 K.

To parameterize the temperature behavior of the dipole relaxation process, the dielectric loss data, ε''(v), collected for all samples were fitted for a temperature range where the relaxation was observed using the sum of the conductivity part and the Cole–Cole equation (which describes the relaxation process visible in Figure 10) [38]:

$$\varepsilon''^{(\omega)} = Im(\varepsilon_\infty + \frac{\Delta\varepsilon}{1+(i\omega\tau)^\alpha}) + \frac{\sigma_{DC}}{\varepsilon_0\omega}, \quad (2)$$

where σ_{DC} is the DC conductivity, α is the shape parameter describing the symmetric broadening of the relaxation curve, $\Delta\varepsilon$ is the dielectric strength, and τ is the relaxation time (the analytical form of this equation used during the fitting procedure is presented in the Appendix A). Representative spectra of ε''(v) for samples with x = 0.0 and 2.0, collected at 178.05 K and 95.38 K, respectively, are presented in Figure 11, together with fitting curves described with Equation (2). The estimated relaxation times as a function of inverse temperature are presented in Figure 12. Because $\tau = f\ (10^3/T)$, the relationships have a linear nature for samples with x = 0.0, 0.4, 1.6, and 2.0, it was possible to parameterize them using the Arrhenius equation: $\tau = \tau_0 \exp(\frac{E_A}{kT})$, where E_A is the activation energy. The estimated value of the activation energy in the intrinsic region E_A = 0.041 ± 0.001 eV for a sample with x = 0.0 was much larger in comparison with samples with x = 0.4 (E_A = 0.024 ± 0.001 eV), 1.6 (E_A = 0.027 ± 0.001 eV), and 2.0 (E_A = 0.025 ± 0.001 eV). This means that the dipole relaxation process was much more sensitive to temperature changes for this sample than for the three other materials. The above activation energy values suggest that activation of the relaxation process in the intrinsic region was much weaker than that of the electrical conductivity. Moreover, from Figures 2 and 12, it is clear that the time scales of the dipole relaxation was the slowest for the sample (x = 0.0) with a higher density and was faster for Mg-doped samples with a lower density. In general, the faster the dipole relaxation, the higher the accumulation of electric charge, which requires a large energy cost. Similar behavior of dielectric relaxation in the scheelite-type $Pb_{1-3x}\square_xGd_{2x}(MoO_4)_{1-3x}(WO_4)_{3x}$ materials (x = 0.0455, 0.0839, 0.1154, 0.1430, 0.1667, and 0.1774, where □ denotes vacancies) was observed. In the above-mentioned Gd-doped lead molybdato-tungstates for poorer gadolinium samples with a lower density, the dipole relaxation was faster, while for samples richer in gadolinium with a higher density, the relaxation process was slower [39]. This finding confirms previous conclusions derived from the analysis of the data presented in Figure 10. The level of porosity of $p_l \approx 1.67\%$, visible in Figure 2, weakly depended on the magnesium content and had no significant effect on the relaxation processes in the materials under study.

It is important to notice that the sample with x = 1.0 shows exceptional behavior for $\tau(10^3/T)$ (Figure 12). This may be associated with the very low residual conductivity with non-linearly increasing energy activation (Figure 3) and low electron emission at 300 and 400 K, which is visible in the I–V characteristics (Figure 5a,b). In particular, for this material, two regions with different E_A's can be distinguished. In the low-temperature range below 128 K, i.e., in an extrinsic region, E_A = 0.017 (± 0.003) eV was estimated, whereas in the high-temperature limit, i.e., in an intrinsic region, E_A = 0.084 (± 0.004) eV. This suggests that some kind of transition took place in the vicinity of T ≈ 128 K, which is not very far from the 109 K where the change in the ε_r(T) dependence was observed for this material (see the inset in Figure 8b for x = 1.0). For another sample (excluding x = 0.0), the relaxation process was much faster. Consequently, the transitions remained invisible, most probably because it was located in the temperature range in which the relaxation process remained out of or just at the end of the experimental window. In the case of the sample with x = 0.0, the transition took place at ≈90 K (see the inset in Figure 8a for x = 0.0), and consequently, should take place for relaxation times longer than the times accessible in these experiments.

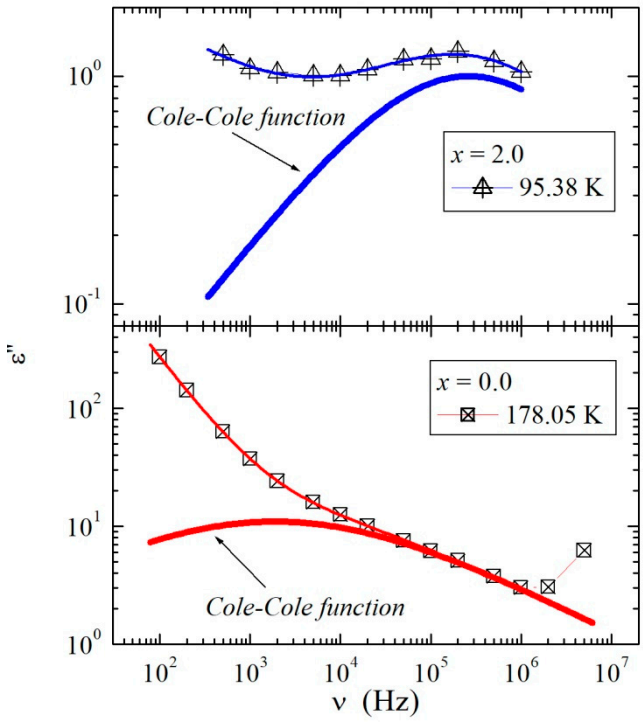

Figure 11. ε″(ν) spectra with fitting function for samples with x = 2.0 (upper panel) and 0.0 (lower panel).

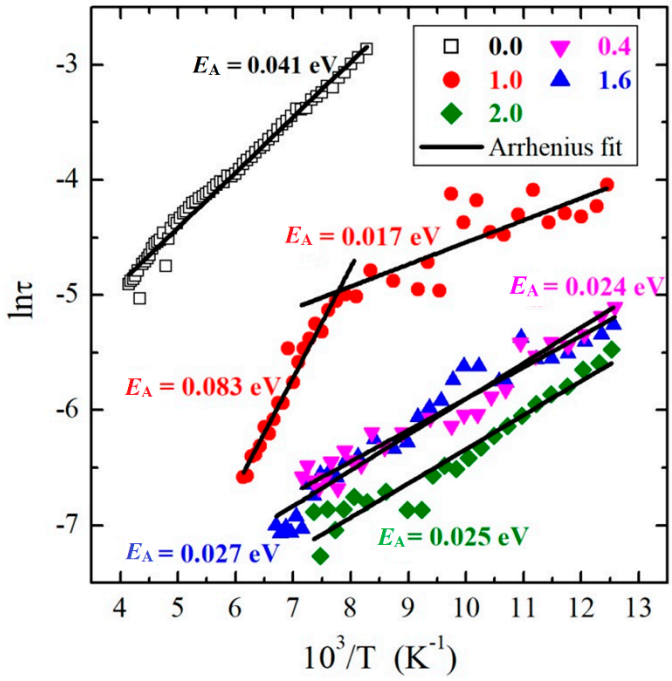

Figure 12. Arrhenius plot of the dielectric relaxation times, τ, for various samples. Straight (black) lines represent fits with constant activation energies, E_A.

4. Conclusions

In summary, $Zn_{2-x}Mg_xInV_3O_{11}$ (x = 0.0, 0.4, 1.0, 1.6, and 2.0) materials were characterized in terms of electrical conductivity, thermoelectric power, I–V characteristics, and broadband dielectric spectroscopy measurements. They have shown *n*-type semiconducting properties and low electron emissions at 300 and 400 K, as well as a strong dependence on the temperature, frequency, and magnesium content of the relative dielectric constant and loss tangent. It should be highlighted

that the temperature dependence of the resistivity can be very well described over a broad temperature range using the parallel resistor model. Moreover, DFT calculations showed that these materials exhibited a non-magnetic and semiconducting ground state. The width of the bandgap increased with increasing Mg content.

The dipole relaxation process in the dielectric loss spectra of $Zn_{2-x}Mg_xInV_3O_{11}$ was analyzed using the sum of the DC conductivity part and the Cole–Cole function. It was established that the dipole relaxation was the slowest for the sample (x = 0.0) with a higher density and became faster for Mg-doped samples (x > 0.0) with a lower density. Moreover, in the case of the sample with x = 1.0, a rather sharp change in the temperature dependence of dipole relaxation times, characterized by markedly different activation energies, was observed. It should be stressed that the faster the dipole relaxation, the greater the accumulation of electric charge. Furthermore, the relaxation time strongly depended on the magnesium content and sample density, and poorly on its porosity. The most interesting result of the studied compounds was that the weaker activation of relaxation processes made electronic transport easier in the intrinsic (semiconducting) region. The strong temperature- and frequency-dependent permittivity and high dielectric losses make these materials a poor choice as a dielectric in a typical electric capacitor. On the other hand, these materials, due to their very high thermopower over a broad temperature range and high resistivity can be used in temperature sensors that will not heat themselves due to current flow (conventional resistive sensors always heat themselves due to current flow). Thermocouples made from metallic alloys also have high thermal conductivity and much lower thermopower (at relatively low temperatures), which makes the precise measurement of the temperature of small samples difficult due to heat conduction. We see the potential application of such materials in temperature sensors used in calorimeters to measure, e.g., the electrocaloric effects at low and moderate temperatures. There exist materials with high thermopowers at low temperatures (e.g., Kondo insulators) but they do have a relatively high thermal conductivity. These compounds, due to their low symmetry and many inequivalent atomic sites, should exhibit high phonon scattering, and consequently, low thermal conductivity.

Author Contributions: Conceptualization, T.G. and B.S.; methodology, T.G., B.S., S.P., and H.D.; validation, T.G.; formal analysis, S.P., T.G., and A.N.; investigation, T.G., M.B., E.F., S.P., A.N., B.S., H.D., and J.G.; resources, E.F. and T.G.; writing—original draft preparation, T.G., E.F., S.P., and J.G.; writing—review and editing, T.G., E.F., S.P., and M.B.; visualization, T.G. and S.P.; supervision, T.G. and J.G.; project administration, T.G. and E.F. All authors have read and agreed to the published version of the manuscript.

Funding: This research received no external funding.

Acknowledgments: This work was partly supported by the Ministry of Science and Higher Education (Poland) and funded from Science Resources (No. 1S-0300–500-1-05-06 and UPB-DZS 518-10-020-3101-01/18).

Conflicts of Interest: The authors declare no conflict of interest.

Appendix A

The Cole–Cole function for fitting the dielectric loss relaxation process:

$$\varepsilon''(\omega) = \Delta\varepsilon\left[1 + 2(\omega\tau)^{\alpha} sin(\frac{\pi\alpha}{2}) + (\omega\tau)^{2\alpha}\right]^{-\frac{1}{2}} sin\varphi \quad (3)$$

where

$$\varphi = arctan\left[\frac{(\omega\tau)^{\alpha} sin(\frac{\pi\alpha}{2})}{1 + (\omega\tau)^{\alpha} cos(\frac{\pi\alpha}{2})}\right] \quad (4)$$

References

1. Wang, X.; Vander Griend, D.A.; Stern, C.L.; Poeppelmeier, K.R. Structure and cation distribution of new ternary vanadates $FeMg_2V_3O_{11}$ and $FeZn_2V_3O_{11}$. *J. Alloys Compd.* **2000**, *298*, 119–124. [CrossRef]
2. Kurzawa, M.; Blonska-Tabero, A.; Rychlowska-Himmel, I.; Tabero, P. Reactivity of $FeVO_4$ towards oxides and pyrovanadates (V) of Co and Ni. *Mater. Res. Bull.* **2001**, *36*, 1379–1390. [CrossRef]

3. Kurzawa, M.; Rychlowska-Himmel, I.; Blonska-Tabero, A.; Bosacka, M.; Dabrowska, G. Synthesis and characterization of new compounds $Ni_2CrV_3O_{11}$ and $Zn_2CrV_3O_{11}$. *Sol. State Phenom.* **2003**, *90–91*, 347–352. [CrossRef]
4. Kurzawa, M.; Rychlowska-Himmel, I.; Bosacka, M.; Dabrowska, G. A new compounds $Mg_2CrV_3O_{11}$ and phase relations in the MgV_2O_6–$MgCr_2O_4$ system in the solid state. *Sol. State Phenom.* **2003**, *90–91*, 353–358. [CrossRef]
5. Bosacka, M. The synthesis and selected properties of new double vanadates $M_2InV_3O_{11}$, where M = Zn, Mg. *Mater. Res. Bull.* **2006**, *41*, 2181–2186. [CrossRef]
6. Bosacka, M. The synthesis and selected properties of $Co_2InV_3O_{11}$. *J. Therm. Anal. Calorim.* **2007**, *88*, 43–46. [CrossRef]
7. Trukhanov, A.V.; Kostishyn, V.G.; Panina, L.V.; Korovushkin, V.V.; Turchenko, V.A.; Thakur, P.; Thakur, A.; Yang, Y.; Vinnik, D.A.; Yakovenko, E.S.; et al. Control of electromagnetic properties in substituted M-type hexagonal ferrites. *J. Alloys Compd.* **2018**, *754*, 247–256. [CrossRef]
8. Trukhanov, S.V.; Trukhanov, A.V.; Turchenko, V.A.; Trukhanov, A.V.; Trukhanova, E.L.; Tishkevich, D.I.; Ivanov, V.M.; Zubar, T.I.; Salem, M.; Kostishyn, V.G.; et al. Polarization origin and iron positions in indium doped barium hexaferrites. *Ceram. Int.* **2018**, *44*, 290–300. [CrossRef]
9. Almessiere, M.A.; Trukhanov, A.V.; Slimani, Y.; You, K.Y.; Trukhanov, S.V.; Trukhanova, E.L.; Esa, F.; Sadaqat, A.; Chaudhary, K.; Zdorovets, M.; et al. Correlation Between Composition and Electrodynamics Properties in Nanocomposites Based on Hard/Soft Ferrimagnetics with Strong Exchange Coupling. *Nanomaterials* **2019**, *9*, 202. [CrossRef]
10. Bosacka, M.; Filipek, E. New continuous solid solution in the $Zn_2InV_3O_{11}$–$Mg_2InV_3O_{11}$ system. *J. Therm. Anal. Calorim.* **2017**, *130*, 63–68. [CrossRef]
11. Groń, T.; Blonska-Tabero, A.; Filipek, E.; Urbanowicz, P.; Sawicki, B.; Duda, H.; Stokłosa, Z. Electrical transport properties of $M_2FeV_3O_{11}$ (M = Mg, Zn, Pb, Co, Ni) ceramics. *Ceram. Int.* **2017**, *43*, 6758–6764. [CrossRef]
12. Orel, B.; Surca Vuk, A.; Opara Krasovec, U.; Drazic, G. Electrochromic and structural investigation of $InVO_4$ and some other vanadiabased oxide films. *Electrochim. Acta.* **2001**, *46*, 2059–2068. [CrossRef]
13. Cimino, N.; Artuso, F.; Decker, F.; Orel, B.; Surca Vuk, A.; Zanoni, R. XPS and IR studies of transparent $InVO_4$ films upon Li charge–discharge reactions. *Sol. State Ion.* **2003**, *165*, 89–96. [CrossRef]
14. Miyata, T.; Minami, T.; Shimokawa, K.; Kakumu, T.; Ishii, M. New materials consisting of multicomponent oxides for thin-film gas sensors. *J. Electrochem. Soc.* **1997**, *144*, 2432–2436. [CrossRef]
15. Müller, C.; Müller-Buschbaum, H. Zur Kenntnis von $Mg_{2-x}Zn_xGaV_3O_{11}$ (x = 0.3). *J. Alloys Compd.* **1992**, *185*, 163–168. [CrossRef]
16. Abello, L.; Husson, E.; Repelin, Y.; Lucazeau, G. Vibrational spectra and valance force field of crystalline V_2O_5. *Spectrochim. Acta. A* **1983**, *39*, 641–651. [CrossRef]
17. Sawicki, B.; Bosacka, M.; Filipek, E.; Groń, T.; Duda, H.; Oboz, M.; Urbanowicz, P. Effect of magnesium substitution on dielectric constant of $Zn_{2-x}Mg_xInV_3O_{11}$ (x = 0.0, 0.4, 1.6) solid solutions. *Acta. Phys. Pol. A* **2018**, *134*, 958–961. [CrossRef]
18. Dovesi, R.; Erba, A.; Orlando, R.; Zicovich-Wilson, C.M.; Civalleri, B.; Maschio, L.; Rerat, M.; Casassa, S.; Baima, J.; Salustro, S.; et al. Quantum-mechanical condensed matter simulations with CRYSTAL. *WIREs Comput. Mol. Sci.* **2018**, *8*, 1360. [CrossRef]
19. Rothballer, J.; Bachhuber, F.; Rommel, S.M.; Söhnel, T.; Weihrich, R. Origin and effect of In–Sn ordering in InSnCo3S2: A neutron diffraction and DFT study. *RSC Adv.* **2014**, *4*, 42183–42189. [CrossRef]
20. Vilela Oliveira, D.; Peintinger, M.F.; Laun, J.; Bredow, T. BSSE-correction scheme for consistent gaussian basis sets of double- and triple-zeta valence with polarization quality for solid-state calculations. *J. Comput. Chem.* **2019**, *40*, 2364–2376. [CrossRef] [PubMed]
21. Perdew, J.P.; Chewary, J.A.; Vosko, S.H.; Jackson, K.A.; Pederson, M.R.; Singh, D.J.; Fiolhais, C. Atoms, molecules, solids, and surfaces: Applications of the generalized gradient approximation for exchange and correlation. *Phys. Rev. B* **1992**, *46*, 6671–6687. [CrossRef] [PubMed]
22. Sawicki, B.; Groń, T.; Tomaszewicz, E.; Duda, H.; Górny, K. Some optical and transport properties of a new subclass of ceramic tungstates and molybdates. *Ceram. Int.* **2015**, *41*, 13080–13089.
23. Wiesmann, H.; Gurwitch, M.; Lutz, H.; Ghosh, A.K.; Schwarz, B.; Strongin, M.; Allen, P.B.; Halley, J.W. Simple Model for Characterizing the Electrical Resistivity in A−15 Superconductors. *Phys. Rev. Lett.* **1977**, *38*, 782–785. [CrossRef]

24. Goraus, J.; Ślebarski, A.; Fijałkowski, M. Electronic and thermal properties of non-magnetic CeRhGa. *J. Alloys Compd.* **2011**, *509*, 3735–3739. [CrossRef]
25. Goraus, J.; Kubacki, J.; Czerniewski, J.; Fijałkowski, M. Cisplatin-A new wide bandgap semiconductor. *J. Alloys Compd.* **2020**, *817*, 153270–153276. [CrossRef]
26. Ślebarski, A.; Goraus, J. Electronic structure and thermodynamic properties of Fe_2VGa. *Phys. Rev. B* **2009**, *80*, 235121–235130. [CrossRef]
27. Von Hippel, A. *Dielectrics and Waves*; Artech House: London, UK, 1995; p. 228.
28. Jonscher, A.K. *Dielectric Relaxation in Solids*; Chelsea Dielectric Press: London, UK, 1983; p. 310.
29. Groń, T.; Filipek, E.; Pacześna, A.; Urbanowicz, P.; Sawicki, B.; Duda, H. Electrical Properties of $Sr_2InV_3O_{11}$. *Acta Phys. Pol. A* **2016**, *130*, 1239–1241. [CrossRef]
30. Groń, T.; Filipek, E.; Piz, M.; Duda, H. Conductance in $Nb_6VSb_3O_{25}$—A new ceramic compound. *Mater. Res. Bull.* **2014**, *51*, 105–108. [CrossRef]
31. Groń, T.; Filipek, E.; Piz, M.; Kukuła, Z.; Pawlus, S. Electric relaxation in $Nb_6VSb_3O_{25}$–ceramics. *Acta Phys. Pol. A* **2016**, *129*, 355–358. [CrossRef]
32. Simmons, J.G. Poole-Frenkel effect and Schottky effect in metal-insulator-metal systems. *Phys. Rev.* **1967**, *155*, 657–660. [CrossRef]
33. Li, C.; Wang, J.; Su, W.; Chen, H.; Wang, W.; Zhuang, D. Investigation of electrical properties of $SnO_2{\cdot}Co_2O_3{\cdot}Sb_2O_3$ varistor system. *Phys. B* **2001**, *307*, 1–8. [CrossRef]
34. Groń, T.; Filipek, E.; Piz, M.; Duda, H.; Mydlarz, T. I–V characteristics in Nb_2VSbO_{10}–ceramics. *Mater. Res. Bull.* **2013**, *48*, 2712–2714. [CrossRef]
35. Groń, T.; Tomaszewicz, E.; Kukuła, Z.; Pawlus, S.; Sawicki, B. Dielectric permittivity of some novel copper/cobalt and rare-earth metal tungstates. *Mater. Sci. Eng. B* **2014**, *184*, 14–17. [CrossRef]
36. Kukuła, Z.; Tomaszewicz, E.; Mazur, S.; Groń, T.; Duda, H.; Pawlus, S.; Kaczmarek, S.M.; Fuks, H.; Mydlarz, T. Dielectric and magnetic permittivities of three new ceramic tungstates $MPr_2W_2O_{10}$ (M = Cd, Co, Mn). *Philos. Mag.* **2012**, *92*, 4167–4181. [CrossRef]
37. Wübbenhorst, M.; van Turnhout, J. Analysis of complex dielectric spectra. I. One dimensional derivative techniques and three-dimensional modeling. *J. Non-Cryst. Solids* **2002**, *305*, 40–49. [CrossRef]
38. Kalmykov, Y.P.; Coffey, W.T.; Crothers, D.S.F.; Titov, S.V. Microscopic Models for Dielectric Relaxation in Disordered Systems. *Phys. Rev. E* **2004**, *70*, 041103.
39. Kukuła, Z.; Maciejkowicz, M.; Tomaszewicz, E.; Pawlus, S.; Oboz, M.; Groń, T.; Guzik, M. Electric relaxation of superparamagnetic Gd-doped lead molybdato-tungstates. *Ceram. Int.* **2019**, *45*, 4437–4447. [CrossRef]